Mechanical characterization of yarns made from carbon nanotubes for the instrumentation of particle beams at CERN

Alexandre Mariet, Ana Teresa Perez Fontala, Xavier Gabrion, C Salomon, Raymond Veness, Michel Devel

Mechanical characterization of yarns made from carbon nanotubes for the instrumentation of particle beams at CERN

A. Mariet, A. T. Perez Fontenla, R. Veness

CERN, Esplanade des Particules 1, 1211 Geneva, Switzerland

X. Gabrion, M. Devel

FEMTO-ST institute (UBFC, CNRS), ENSMM, 15B avenue des Montboucons, 25030 Besançon CEDEX, France

C. Salomon

Polytech Annecy-Chambéry, University Savoie Mont Blanc, 74940 Annecy, France

Abstract

Existing copper-coated carbon fibers used in wire scanners to measure the transverse beam profile in the accelerators at CERN are approaching material limits. A new instrument design has showed that the main limitation now comes from the centerpiece of the instrument: the wire. Large amplitude vibrations increase the risk of failure during scans. New required specifications concerning the beam measurements for the Future Circular Collider (FCC) project cannot be met. Fortunately, the commercial development of long microscopic yarns made of spun carbon nanotubes has paved the way for possible alternatives. The objective of this study is to determine if those Carbon NanoTube Yarns (CNTY) could replace the current carbon fibers (CF) for beam instrumentation, and if so, to determine the best configuration in terms of diameters and mounting system. To do so, we have made extensive testing and microscopy on CNT yarns with diameters of 10, 20 and 30 µm, with two different mounting systems, the Paper Frame conditioning (PF) or partial Copper-Coated conditioning (CC). A Weibull approach was used to extrapolate our results to the real length of the wires used in operational instruments. This study shows that considering the Weibull criteria, the best configuration to increase the accuracy of the beam profile measurement is to

Preprint submitted to Nuclear Inst. and Methods in Physics Research, A March 25, 2022

use a not copper-coated 20 µm diameter CNTY.

Keywords: Carbon nanotube, CNT yarn, material, wire-scanner, beam instrumentation, tensile test, failure strength, Weibull

1. Introduction

In high-energy physics, physicists are pushing for an increase in beam energy and intensity as well as smaller beam sizes. New technically challenging projects are planned. The LHC Injector Upgrade (LIU) [1], High Luminosity LHC Project (HL-LHC) [2] and Future Circular Collider (FCC) [3] will improve the beam brightness at CERN in the next years. Wire-scanners (WS) are devices used since the 1980s [4, 5] to measure the transverse beam density profile, by moving a thin wire across the particle beam and detecting the secondary particles. The interaction between the beam and the wire creates secondary particle showers with an intensity proportional to the number of particles crossing the wire. These secondary particles are intercepted by a scintillator positioned downstream of the wire, coupled to a photo-multiplier which amplifies the resulting signal. The acquisition of the wire position and the signal intensity are combined to reconstruct the transverse beam density profile. The first WS moved linearly with stepper motor [6, 7] which required very low scan speeds, of up to 1 $m.s^{-1}$ [8, 9]. Various studies on this instrument were carried, from the influence of the diameter of the wire [10] to its thermal behavior[7, 11, 12]. Another generation of rotary WS was then designed to meet higher specifications [13] in the Proton Synchrotron Booster (PSB) and the Proton Synchrotron (PS). However, in the coming years, the beam will progressively be smaller and more intense. This will lead to two main issues with the current generation of WS: an overheating of the wire [14–16] and an insufficient resolution for the beam size. In order to address the overheating issue, a new generation of fast wire-scanners [17, 18] was developed at CERN (Fig 1), for the whole accelerator chain, from PSB to the Super Proton Synchrotron (SPS). The whole engineering concept has been redesigned with new machining and manufacturing concepts [19, 20]. The major improvement is the increase of the scan velocity up to 20 $m.s^{-1}$, which allows to reduce the beam/wire interaction time and consequently the increase of temperature. Everything in this new WS was changed, except the centerpiece of the instrument: the wire. The same material with the same mounting system has been used from the beginning, i.e. partially

copper coated carbon fiber. The problem is that first, most common wires (carbon fiber, gold coated tungsten,...) will be destroyed in the HL-LHC conditions[15] and second, the precision of the wire installation is currently mainly dependent on the technicians who install the wire manually and is prone to large variations in the calibration results.

As an alternative to conventional carbon fibers, we considered fibers made of Carbon NanoTubes (CNT), a new exciting material formed by one (Single Wall Carbon NanoTube - SWCNT) or several (Multi Wall Carbon NanoTube - MWCNT) sheets of graphene, coiled on themselves. It seems that such nanotubes were already observed in the 50s [21] but really highlighted only 30 years later, by Sumio Iijima [22]. For isolated nanotubes, experimental studies and theoretical simulations showed a combination of excellent mechanical [23–25], electrical [26–29], and thermal properties [30–32]. Its very light weight for a solid, with relative densities that can be as low as 0.5, depending on the CNT structure and packing [33] is also an interesting characteristic. The nanometric size, with diameters varying from less than 1 nm for SWCNT [34] to more than 50 nm for the bigger MWCNTs [35] and typical lengths of the order of the micrometer, [35], the millimeter [36–38] or even the centimeter [39], are particularly adapted for new technologies such as nanoelectronics [26, 40] or material composites [27, 41–43]. The "macromechanics" would also be interested in these fabulous characteristics, but individual tubes are not practical for most engineering applications due to their size. More recently, the technology to assemble these tubes together to make long stranded yarns has opened up a new world of potential applications. Different methods were developed such as dry spinning [44], wet spinning [45, 46], in situ direct spinning [34] and spinning from gas phase [47] that offer a wide panel of possible configurations.

Many academic institutes and industrial companies are interested in investing and developing these new Carbon NanoTube Yarns (CNTY) further. Nevertheless, several studies [48–50] showed a large difference between the properties of a single nanotube and the properties of the wire assembly. Indeed, the bonds between carbon atoms inside the coiled graphene layers are strong covalent bonds, whereas the inter-tubes bonds inside the wire are weak van der Waals forces. It led to a disappointment for some applications needing high mechanical properties and a microscale structure. Methods to improve the mechanical properties of pristine yarns exist such as chemical treatment [51–53] or densification by twisting [54–56]. However, the influence of a partial copper-coating on the mechanical properties has not been stud-

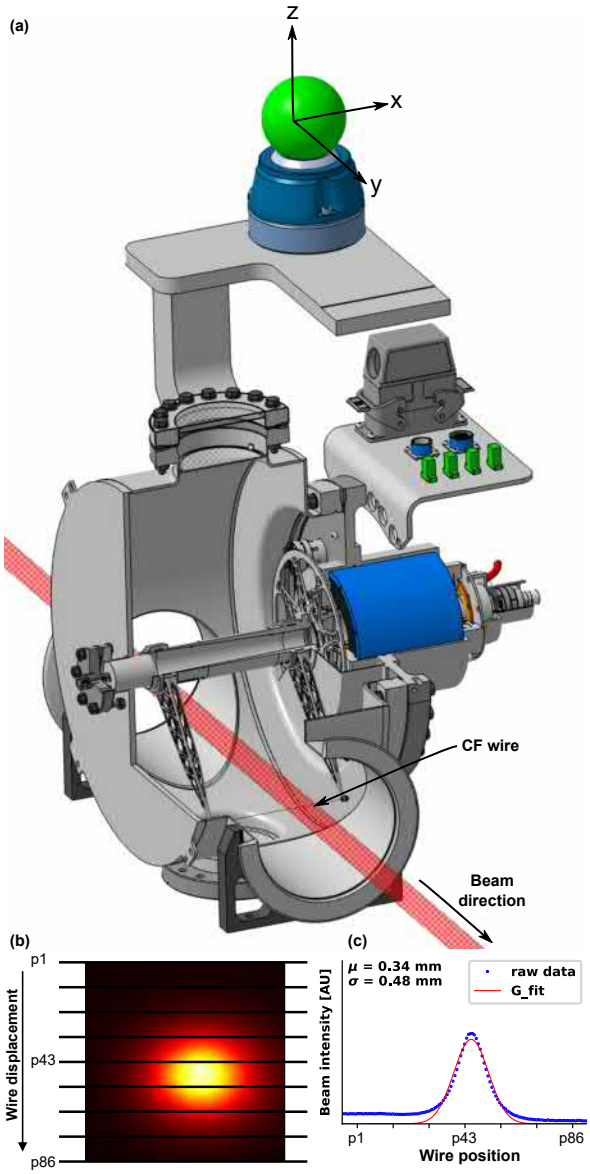

Figure 1: (a) 3D CAD model of the new generation of fast wire-scanners (WS) for SPS, (b) illustration of the wire vertical movement and interaction with the beam. During a scan, the wire crosses 86 times the beam for a beam size of 500 µm and a scan speed of 20 m.s^{-1}, represented here by p1–p86. (c) Beam profile reconstruction combining the signal, proportional to the number of interactions, and the wire position.

ied. Hence, the goal of our study is to determine the best configuration for this new material considering several diameters (10, 20 and 30 µm), and two different mounting systems: 1- glued on a paper frame (PF) and 2- partially copper coated (CC). This new input will be carefully analyzed and will be determinant for the upgrade of the wire scanners used at CERN.

We will first describe the material, methods and protocols used, then describe the results of our measurements and the Weibull analysis done to estimate the maximum tensile stress that we will be able to impose safely to the yarns during their installation on wire scanners of the new generation. This point is crucial to achieve fast scan speeds with minimal deformations as required to monitor with a sufficient precision the beam profile in enhanced luminosity conditions. An in-depth discussion of our results, with a comparison with other results from the literature will then lead us to give some perspectives and propose recommendations for the configuration to be used at CERN.

2. Material, methods and protocols

2.1. Preparation of the tensile tests

The wires used for this study were provided by Hitachi Zosen Corporation. CNTs were obtained by Chemical Vapor Deposition, producing a vertically aligned sheet. [57–59]. The as-grown CNTs have an outer diameter of 10 to 12 nm. These are typical values which can be found in many productions [44]. The average number of walls composing the tubes are between 5 and 10. Yarns were then obtained by spinning CNTs sheets.

The nominal diameters of the wires that we used for our mechanical tests were 10, 20 and 30 µm, but were measured with an electron microscope (SEM) to be 12.71 ± 0.32, 21.95 ± 0.32 and 32.43 ± 0.27 µm respectively. The real cross-section areas were measured to be $127 \pm 7, 379 \pm 13$ and 826 ± 14 µm^2 respectively, which are very close to values that can be computed for circular cross-sections. The twist angles were measured at $16 \pm 1°$, $20 \pm 2°$ and $19 \pm 1°$ for wires of 10, 20 and 30 µm respectively (Table 1). The supplier gives a density between 1.2 and 1.4 g.cm^{-3} for the yarns. Because of the limited amount of available yarns and technical problems, we could not measure the density of the yarns with nominal diameters 10, 20 and 30 µm. However, for a 100 µm CNTY sample, we measured with an hydrostatic balance based on Archimedes' principle a density of 1.3 ± 0.2 g.cm^{-3}, which we used in our mechanical simulations (and a density of 1.7 g.cm^{-3} for 34 µm carbon fibers).

Table 1: Real measured diameters and twist angles

	ø[µm]	α [°]
10 µm	12.71 ± 0.32	16 ± 1
20 µm	21.95 ± 0.32	20 ± 2
30 µm	32.43 ± 0.27	19 ± 1

Our study concerns the effects on the mechanical properties (strain at failure (ε_{max}), tensile strength (σ_{max}), Young's modulus (E) and toughness (T)) of the PF or CC preparations and of the diameters of the wires. Tensile tests were made using a Dynamic Mechanical Analyzer (DMA) (Bose Electroforce3200) at ambient temperature (21 °C) equipped with a 22 N load cell (precision of ± 5 mN) and displacement sensor of ± 1.5 mm (precision of ± 1 µm). The gauge length of the specimens were 10 and 30 mm for the PF and CC preparations, respectively.

Tests were performed with a displacement control at a speed of 1 $mm.min^{-1}$. The Young's modulus quantifies the tensile stiffness of a material. It was determined by linear regression of the stress/strain curves on a range of strain comprised between 0 and 1 %.

As already mentioned, two different mountings have been prepared (PF and CC). For PF, we used a self-adhesive paper frame [60] of 12 mm length. The yarns are positioned across the frame and fixed with a basic cyanoacrylate glue (Fig 2-a). Both sides of the frame are mounted between two aluminum plates and screwed with four M4 screws. To avoid pre-tension in the wire, the assembly is mounted on the clamps before cutting the frame to free the wire (Fig 2-b). CC samples were also tested since wires currently used in WS are coated on the extremities with a layer of copper (350 µm in diameter). This coating allows the soldering of the wire on the forks through a copper insert. It also allows a better electrical conductivity, used to monitor the good state of the wire. A grid is prepared using a classic printed circuit board (Fig 2-c). A thin layer of copper is deposited around the frame. The wires are then stretched by hand, positioned on the frame and fixed by tape. They are glued with a conductive quick curing bi-component epoxy adhesive Epotcny E207. The frame is dipped in an electrolytic bath composed of copper sulfate ($CuSO_4$, 75 $g.l^{-1}$), sulfuric acid (H_2SO_4, 10 % v/v), sodium chloride (NaCl, 0,075 $g.l^{-1}$), copper gleam PC make up (4 $ml.l^{-1}$) and demineralized water. A small current of the order of 1 mA is used. Despite

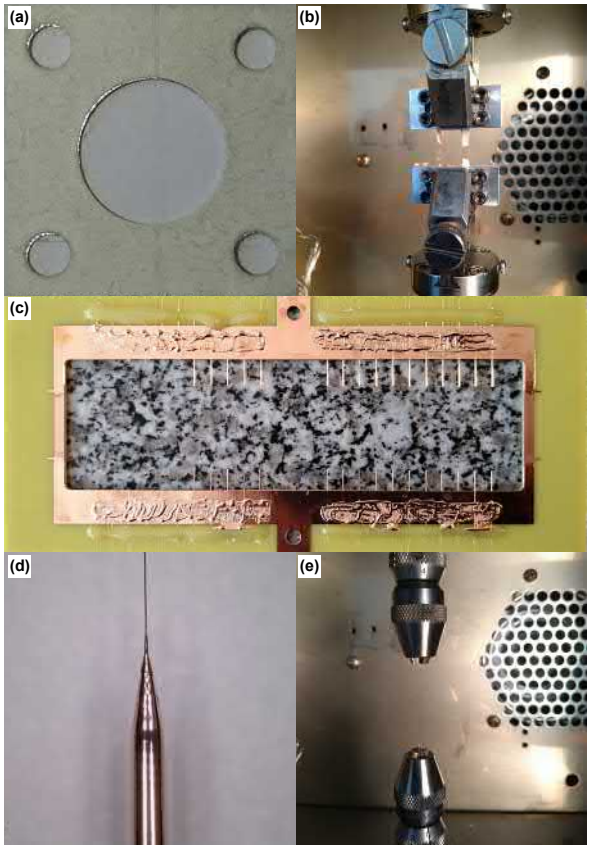

Figure 2: (a) Mounting of the wire on the Paper Frame (PF) and (b) assembly for clamping system in the tensile machine. (c) Typical preparation grid for the copper-coating of the extremities. (d) Quality control of the coating for a yarn of diameter 20 µm and (e) clamping systems for the CC conditioning test

precise specification of the outer diameter of the coating, the complexity of this step implies a wide range in the results (Fig 2-d). To ensure the good alignment of the CC yarns, a cylindrical clamping system has been used (Fig 2-e) .

2.2. Focused Ion Beam (FIB) microscopy

To prepare the samples, mechanical cutting with scissors was performed. The specimens were glued with silver paste to an aluminum stub (standard consumables for SEM). In order to gain improved insight into the microstructure of the CNTs, a cross section was milled by FIB into the samples. For the

transverse cross-section, a 20 (radial) × 2 (axial) × 1 (thickness) µm^3 platinum (Pt) polishing barrier was initially deposited onto the sample surface at a current of 300 pA in order to facilitate effective polishing. A milling current of 3 nA and accelerating voltage of 30 keV were then used to mill out a section using the silicon (Si) ablation ratio. Subsequent polishing milling steps were performed at 700 pA and 100 pA and accelerating voltage of 30 keV and a final polishing was performed at a milling current of 50 pA and accelerating voltage of 30 keV to leave a smooth surface that could be effectively imaged. For the longitudinal cross-section, a milling current of 3 nA and accelerating voltage of 30 keV was used to mill out the material up to approximately half of the wire diameter. Subsequent polishing milling steps were performed at 1.5 nA and 700 pA and accelerating voltage of 30 keV and a final polishing was performed at a milling current of 100 pA and accelerating voltage of 30 keV to leave a smooth surface that could be effectively imaged.

2.3. Analyzing tools

The data analysis was performed by using a combination of Excel worksheets (Microsoft, Redmond, Washington, USA) and python Jupyter Notebooks [61]. Graphs and statistics have been plotted with GraphPad Prism 9 (GraphPad Software, San Diego, California, USA). Images were processed with ImageJ [62] to set up brightness, contrast and get measurements. Figures have been assembled with the free software Inkscape [63]. The void density was calculated using a python script developed internally.

3. Results and discussion

3.1. Internal structure analysis

A CNTY can be described as a hierarchical structure. Individual CNTs self-assemble forming bundles and bundles are bonding together in successive layers to form the final yarn [64]. A good knowledge of the characteristics of the individual CNTs composing the yarn and their packing would be an asset for developing an effective composite model for the yarn [64, 65].

A transverse cross-section has therefore been milled in several yarns using gallium ions from the FIB, to observe their internal structures (see Fig 3-a for the 20 µm yarn). This allows us to measure the packing and the distribution of the CNTs and CNT bundles in the cross-section. For the diameter 20 µm, two sites of interest (SOI) along the diameter have been zoomed in (Fig 3-b). SOI-1 is an area located on the external layer of the yarn (2 µm away from

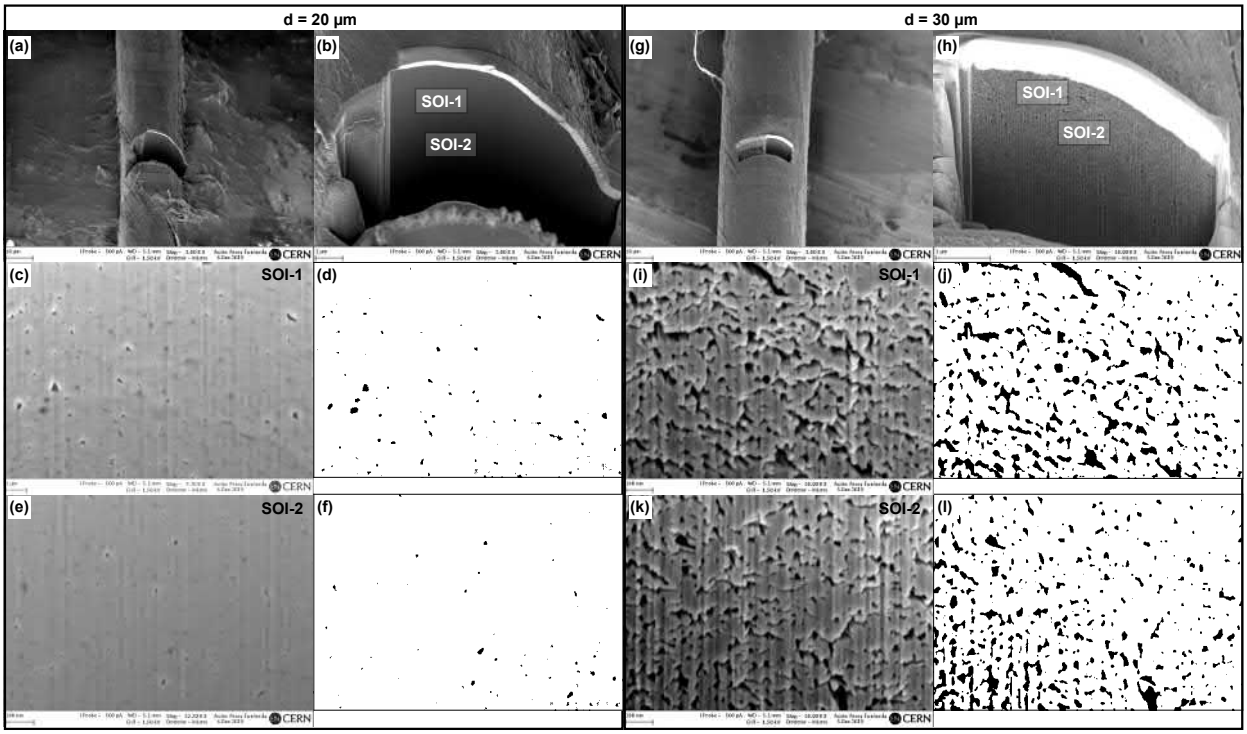

Figure 3: (a) Transverse cross-section of a 20 µm diameter yarn with (b) two sites of interests.(c,d) SOI-1 (outer position) and SOI-2 (inner position) have been zoomed in and (e,f) binarized for the external position with grey level thresholds set at 122 and 110 respectively. (g to l) The same process has been performed for the 30 µm yarn with thresholds of 60 and 45 for SOI-1 and SOI-2 respectively.

the surface). It was observed with a magnification of 7700 (Fig 3-c). This image was binarized (Fig 3-d) from a grey level picture using a threshold manually set to 122 in the python script, in order to visually preserve the extents of the voids while filtering out artifacts. The void density is then estimated by the ratio of black pixels over white pixels. For SOI-1 of the 20 µm yarn, we found 0.63 %. SIO-2 (Fig 3-b) is located at mid distance between the outer part and the center of the layer. A picture was taken with a magnification of 52000 3-e) and binarized 3-f). Using a threshold of 110, the void ratio was then estimated to be 0.28 %.

The same approach has been used for a 30 µm yarn (Fig 3-g), but due to the larger dimensions, only the external diameter area of the wire was prepared by FIB cross section milling. Two sites of interests have been chosen

(Fig 3-h), the first on the external layer of the yarn (Fig 3-i) and the second slightly lower but still on the outer layer (Fig 3-k). Both images have a magnification of 50000. The binarisation gives for SOI-1 a void density of 11 % with a threshold of 60 (Fig 3-j) and 10 % with a threshold of 45 for SOI-2 (Fig 3-l). The cross-section at the external layer of the 30 µm presents a similar aspect in the two sites compared. Groups of well aligned nanotubes are discernible and also, locally, small groups of non-aligned nanotubes are visible in the voids. SOI-1 and SOI-2 had a similar aspect with discernible groups of well aligned nanotubes and also, locally, small groups of non-aligned nanotubes, visible in the voids.

From the above results, we can see that the packing is denser (less voids) for the 20 µm yarns than for the 30 µm yarns, which is in the continuity of the results of a previous study carried out with yarns with diameters varying from 30 to 83 µm [66]. This study showed a decrease of the apparent density from 1.2 to 0.6 g.cm^{-3} with increasing diameter. However, despite the fact that various previous studies showed that the packing of twisted yarns increases with the twist angle [55, 56, 67, 68], our observations do not seem to support this correlation, since we find quite different packings for similar twist angles ($20 \pm 2°$ and $19 \pm 1°$ for wires of 20 and 30 µm respectively (Table 1)). This discrepancy may be due to the non-uniformity of packing in the 30 µm CNTY versus the uniformity of the packing in the 20 µm CNTY. Indeed, we found that the void ratio at the site of interest located on the outer layer of the 20 µm yarn is twice larger than the one at the site of interest located midway between the center and the surface of the yarn. This indicates that for this diameter, the packing is not radially uniform. For the 30 µm, both sites of interest show very similar packings, given the uncertainties inherent to the manual setting of the binarization threshold.

3.2. copper-coating

Wires used in the current wire scanners are copper coated on the extremities for integration reasons. However, coating the yarns with copper is a delicate step in the wire preparation. Therefore, we prepared a new batch of copper-coated wires in order to study the dispersion of their geometrical and mechanical characteristics. Results on the copper-coatings external diameters were very variable compared with the design specifications. They also showed different profiles for a same batch (Fig 4-a). To observe the interface between the yarn and the copper-coating, we performed transverse cross-section using the FIB method. The samples were positioned with the

appropriate angle with silver paste (Fig 4-b). Different levels of zoom were applied (Fig 4-c). The zoom x200 allows a global view and shows the ratio between the diameters of the coating and the yarn. The coating was specified at a diameter of 400 µm to fit in the 500 µm copper insert of the instrument, and is measured at 340 µm. The yarn is very regular and measured at 34.4 µm. Increasing the zoom in, we observe a transition layer between carbon and copper with a thickness of about 5 µm. This transition layer was analyzed by Energy-Dispersive X-ray Spectroscopy which revealed the presence not only of carbon and copper, but also of oxygen and sulfur (Fig 4-d. These last two elements are part of the electrolytic bath of the coating. They are non uniformly distributed in the transition region (Fig 4-e). Chlorine and silicon visible in the spectrum are thought to be measurement artifacts.

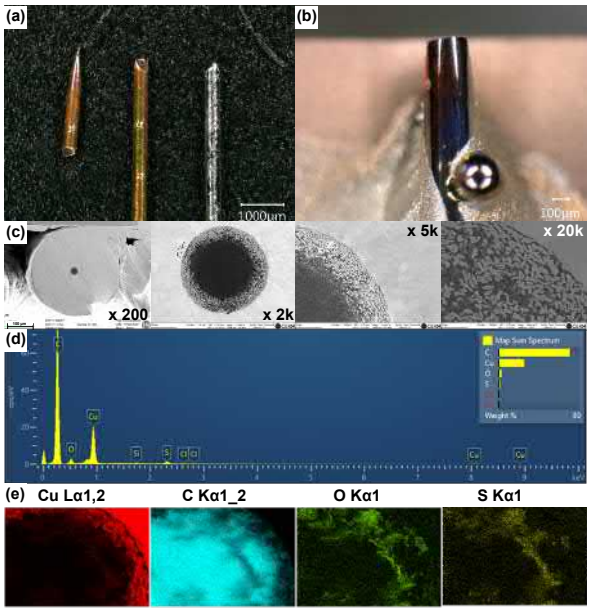

Figure 4: (a) extremities of three yarns, two (left and center) only coated with copper, the third (right) was also welded in silver paste. (b) Samples after FIB milling for cross-section observations. (c) Grey level SEM images of one cross-section at different zoom levels (x200, x2000, x5000 and x20000). copper-coating appears grey while the CNTY appears black. (d) Energy-dispersive X-ray spectrum of a sample highlighting the presence of copper, carbon, oxygen and sulfur. (e) maps of these four elements showing the presence of oxygen and sulfur in the transition region between the inner carbon yarn and the outer copper-coating.

The observation of the interface between the copper-coating and the yarn could lead to the supposition that while filling the voids in the structure of the wire, copper could form new bonds stronger than the weak van der Waals forces between CNTs, which could reinforce the yarn. It would then lead to mechanical properties slightly better than for a pristine yarn, by strengthening the coating region. However, we observed that the strength results of the tensile tests for d20_CC and d30_CC batches are well below the results for the d20_PF and d30_PF batches, which would prevent use of higher tensile forces in order to straighten the wires and, consequently, to improve the accuracy of the WS by decreasing the amplitude of the vibrations. Our FIB/SEM/EDXS observations of cross-sections of CNTYs before tensile tests showed that the coating does not modify the shape of the yarn but that copper penetrates in the superficial layer of the CNTY. However, we have no information on the type of bonds created between the CNTs and the coating. Furthermore, all the samples broke at the end of the copper plating showing that there is probably a stress concentration at this point, leading to a point of weakness. Hence, it seems that partial copper coating is definitely not a good solution from a mechanical perspective. Solutions to improve the mechanical properties by fully coating the wire have been suggested [69], but not adopted in our case. The goal is to reduce the number of interactions with the beam. A coating with a high Z material would lead to an increase of beam interactions. Another alternative solution would be to use iron or tungsten coatings, since these elements are more soluble in carbon than copper and can form carbides, but this solution implies to add an significant mass, which could be a problem. Indeed, a local increase of mass implies larger deflections during the scan due to the acceleration. Moreover, we saw that the reproducibility of the coating process is not very high and is depending on a lot of factors, such as the cleanliness of the tank, precision of the current going through the grid, but also the thickness and the width of the copper layer on the printed circuit board during the grid preparation. This is not acceptable for such a high precision project.

3.3. Mechanical tensile test analysis

3.3.1. Raw parameters calculation

The goal of this study is to find which kind of yarn, with which mounting, could replace the existing carbon fibers used in the current WS. To do so, tensile tests have been performed on 93 samples, combining the two parameters of interest: diameter (10, 20 and 30 µm) and mounting conditioning (PF and CC). Labels and numbers of samples tested are given in Table 2.

Table 2: Labels and numbers of samples for each couple of parameters

	PF	**CC**
10 µm	d10_PF (15)	d10_CC (6)
20 µm	d20_PF (12)	d20_CC (19)
30 µm	d30_PF (16)	d30_CC (25)

Typical raw tensile stress/strain curves show various behaviors for our samples depending on the diameter and conditioning (Fig 5). The left axis of each graph indicates the load (in N) applied to the wire during the test while the right axis is for the corresponding stress (in GPa) calculated as load divided by the previously measured real cross-sections of the yarns. For the CC samples, the diameter used to calculate the stress is also the diameter of the yarn. We consider that the coating parts are part of the clamping system. Looking at the three PF figures corresponding to the three diameters (Fig 5-a, b and c), we can see that the curves are quite similar since they all correspond to a brittle behavior of these non-coated CNTY, with a strain to failure about 2 %. There is a linear increase of the stress between 0 and 90 % of the strain to failure (ε_{max}) and a very short plastic zone before the failure. The behavior for the CC samples is more disparate. Samples from batch d10_CC more or less have the same brittle response as for the PF conditioning, whereas samples of d20_CC and d30_CC batches show a much larger discrepancy between samples, with larger intervals of variation than for the PF conditioning, since the strain at failure varies from 1.4 to 4 % and from 1.7 to 5 % for 20 and 30 µm respectively. The maximal load before the failure also shows large variations, from 140 to 357 mN and from 229 to 638 mN for 20 and 30 µm respectively, corresponding to maximal stresses smaller than in the PF and d10_CC cases.

Strain at failure (ε_{max}), average strength (σ_{max}), Young's modulus (E) and toughness (T) were evaluated from the raw curves of Fig 5.

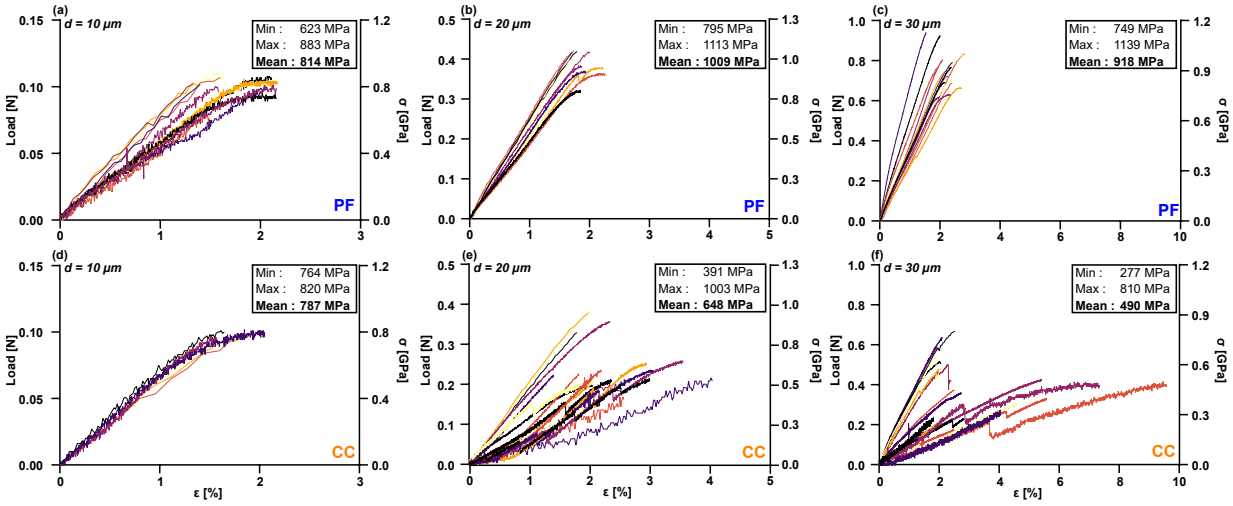

Figure 5: Typical stress / strain curves for the PF (a, b and c) and CC conditionings (d,e and f). For each of these conditionings, response of samples from three different diameters: 10 µm (a and d), 20 µm (b and e) and 30 µm (c and f) have been plotted

Strain at failure. The average strain at failure (ε_{max}) (Fig 6-a) is relatively constant for the PF conditioning for the three diameters, with 1.93 ± 0.54 % for 10 µm, 1.86 ± 0.21 % for 20 µm and 2.28 ± 0.34 % for 30 µm, corresponding to relative variations of 28 %, 11 % and 15 % respectively. For CC conditioning samples, both ε_{max} and its variations seem to increase approximately linearly with the diameter, with slopes of 0.84 and 0.86 respectively.

Stress at failure. The average stress at failure (σ_{max}) for the raw data are shown in Fig 6-b. Comparing the PF and CC conditionings, we can see that results for the 10 µm nominal diameter are the most balanced, with an average fracture stress of 814 ± 65 MPa for PF and 787 ± 22 MPa for CC. The difference between the average fracture stresses of d20_PF (1009 ± 102 MPa) and d20_CC (648 ± 178 MPa) or d30_PF (918 ± 114 MPa) and d30_CC (490 ± 164 MPa) is much larger and correspond to a strong decrease of the fracture stress between the PF and the CC conditionings for these diameters.

Young's modulus. The Young's modulus (E) (Fig 6-c) was calculated using the slope of a linear regression of the stress-strain curve between 0 and 1 % of strain. It is interesting to notice that for the yarns with a nominal 10 µm diameter, the modulus is a larger for CC with 51 ± 3 GPa than for

PF with 44 ± 14 GPa. For the diameters of 20 and 30 µm, it is the opposite, with a modulus for PF twice larger than CC, with 58 ± 7 and 26 ± 15 GPa and 43 ± 11 and 20 ± 12 GPa respectively. We can see that the relative uncertainty is much larger for the d20_CC and d30_CC batches than for the other batches, as already visually evident in Fig 5).

Specific toughness. The specific toughness (T) expressed in J.g^{-1} quantifies the ability of a material to absorb energy by deforming elastically without breaking. It is defined as the area under the stress/strain curve up to the elastic limit, divided by the density. The average specific toughness (Fig 6-d) for the d10_PF batch is 66 ± 18 J.g^{-1}, 78 ± 14 J.g^{-1} for d20_PF and 89 ± 16 J.g^{-1} for d30_PF. These data could be fitted by a linear increase with diameter of equation $T = 1.2d + 54.7$. The yarns with the CC conditioning show another behavior with a specific toughness quite similar for the three diameters, with 62 ± 12, 59 ± 21 and 71 ± 44 J.g^{-1} for d10_CC, d20_CC and d30_CC respectively. We note that for this conditioning, this is the standard deviation which increases linearly.

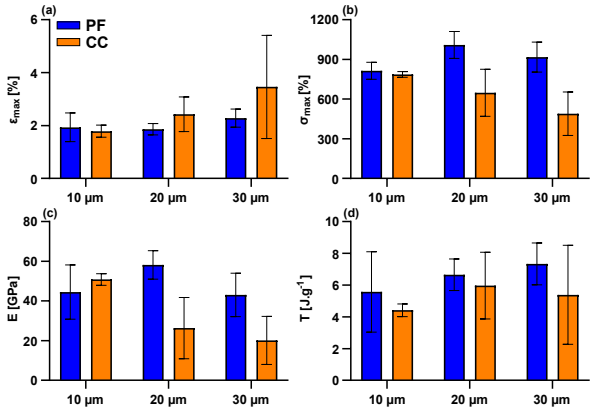

Figure 6: Mechanical parameters synthetis

General comments. The raw data of the stress/strain curves for d10_PF, d20_PF, d30_PF and d10_CC batches show similar behaviors with a linear increase, then some leveling off or linear increase with a smaller slope and finally failure. However, the transition between the two linear regimes varies widely from a sample to another. For the d20_CC and d30_CC batches, some partial fractures appear for some samples and the leveling-off regime is rarely attained. Another difference between batches is that all PF samples

broke in the middle of the yarn while CC samples broke at the extremity of the copper-coating. This indicates that the coating plays a keyrole in the failure mechanism and that the assumption of an improvement due to the filling of the voids is definitely not confirmed. An explanation may be that the coating on both extremities over-constrains the outer layers. Under the tension, the external layers break first which induces the successive partial fails before the final failure. With decreasing the diameter, the coating could stress more homogeneously the yarn which may lead to a single and abrupt failure.

3.3.2. Weibull parameters calculation

For many years, scaling models for composite materials have been the subject of intense research. Empirical, phenomenological or progressive damage methods, all aim to optimize and improve the performances of these materials [70]. Our study also fits in this framework, with the idea of testing small-sized samples of short CNTYs and adapting the results to the longer wires used in wire scanners, using Weibull methods. Main tests are performed with small gauge length samples [71, 72] as limits on translational stroke of the tensile machine does not accommodate samples of length used in WS. This kind of analysis allows scaling the dispersion of the mechanical strength results without explicitly modeling the defects, using the hypothesis that a higher degree of similarity of defect type and uniformity results in a smaller dispersion of failure stresses. In this approach, the state of the material (failed or not) is represented by a random variable which is distributed according to a probability law that depends on the applied stress and can be experimentally identified by a series of tests (see e.g. [73, 74]). The probability of survival follows a Weibull distribution and is then expressed as [75, 76]:

$$P_s(\sigma) = \exp\left[-V^*\left(\frac{\sigma}{\sigma_0}\right)^m\right] \tag{1}$$

where σ is the applied stress, σ_0, the scale parameter, and m the shape parameter (Weibull modulus). V^* is the reduced volume equal to the actual volume divide by a reference volume. First, to get the scale and shape parameters, we consider that the volume of reference is the volume of the sample, so that $V^* = 1$. In order to compute σ_0 and m, we first sort the samples by stress at failure (σ_{max}) from lowest to highest. Each sample then has an associated probability of survival that can be evaluated using its rank in the

list (n_{rank}) with formulas that depend on the number of samples ($N_{samples}$). For moderate size samples [76]

$$P_s(\sigma_{max}) = 1 - \frac{n_{rank}(\sigma_{max}) - 0.3}{N_{samples} + 0.4} \tag{2}$$

Then (for $V^* = 1$), we can obtain m and σ_0 thanks to a linear fit using the following equation derived from Eq. 1

$$\ln(-\ln(P_s))) = m\ln(\sigma_{max}) - m\ln(\sigma_0) \tag{3}$$

Indeed, using a plot (Fig 7) of $\ln(-\ln(P_s))$ as a function of $\ln(\sigma)$, the slope of the linear regression gives the modulus m and the Y-intercept y_0 gives $\sigma_0 = \exp(y_0/m)$. Results for m and σ_0 for the three diameters and two conditionings, are summarized in Table 3 along with r^2 which characterizes the quality of fit.

For the 10 µm batches, Weibull moduli are 19.18 and 28.11 respectively, for PF and CC conditionings. This is quite high compared with the results for the 20 and 30 µm batches (between 3.05 and 8.25). This is normal since a mathematically known property of the Weibull modulus is that the lower m, the greater the dispersion of the variable characteristic of the failure. This has been seen for composite materials with fibers oriented at random, lower values of m corresponded to greater dispersions of the tensile strength. Hence, the high m for the low diameter indicates a defects distribution more homogeneous than for the larger diameters, which agrees with the previous observations of the packing.

The results for σ_0 show 6 % of difference between the PF and the CC conditionings for the diameter of 10 µm, while this difference increases up to 32 % for the 20 µm batches and 43 % for the 30 µm batches. The r^2 values indicate a fair quality of the linear fits, with a minimum of 0.88 for the d20_CC batch and a maximum of 0.96 for the d30_PF batch. In order to compare the new CNT yarns with the existing CF wires, other tests have been performed with 8 samples of carbon fibers (as used in current WS) of diameter 34 µm and length 10 mm, with a PF conditioning only. Results for those tests are summarized in the last line of Table 3, in italic. they give a modulus of 11.8 and a σ_0 of 928 MPa. With $r^2 = 0.93$, the fit is as good as for the CNT yarns.

Our study for diameters from 10 to 30 µm, completes the study of Sugano et al. [66] in which 4 yarns with diameters larger than 30 µm were used.

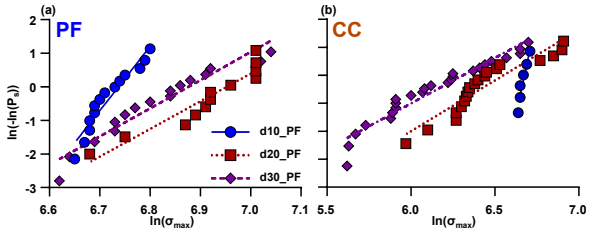

Figure 7: Linear fits of results of tensile tests using a Weibull failure probability law. (left) PF samples, (right) CC samples

Table 3: Weibull parameters m and σ_0 and goodness of fit r^2

	m		**σ_0 [MPa]**		**r^2**	
ø	**PF**	**CC**	**PF**	**CC**	**PF**	**CC**
10	19.8	28.1	843	793	0.92	0.91
20	8.3	3.6	1045	700	0.90	0.88
30	7.7	3.1	957	537	0.96	0.96
34	*11.8*	-	*928*	-	*0.93*	-

They found a decrease of the shape parameter m from 9.4 to 3.1, and scale parameter σ_0 from 938 to 217 MPa with the increase of the diameter, which is coherent with our results.

3.3.3. Operational parameter calculation

The interest of this study is to verify if these new yarns could be installed on operational WS. If so, the length of the yarns will not be 12 or 30 mm as in the tests, but 150 mm. In order to extrapolate our experimental results to yarns of 150 mm, Weibull analysis is a good approach, since the stress-strain curves showed a brittle behavior, sometimes with significant variations, which excludes using the classic sizing criteria used for ductile materials [77–79]. Furthermore, CNTYs broke at maximal stresses (σ_{max}) which varied greatly from a sample to another, particularly for the d20_CC and d30_CC batches. This dispersion, probably due to the presence of defects in variable quantities and distributions, undermines the classical assumption of homogeneity of mechanical behavior.

To make this extrapolation, we used an equivalent reduced volume V^* expressed as $V^* = V_{\text{op}}/V_{\text{sample}}$, with V_{op} the volume of the operational wire and V_{sample} the volume of the samples used for the mechanical tests [80], either

for PF or CC conditionings. Using Eq.1, we see that the larger the operational volume, the smaller the survival probability, which is normal since the number of defects is increased. In fact, we can also define $V^* = 150/l_{cond}$, since the wires in the operational future WS will have one of the diameters used during the tests and consequently the same cross-section as the CNTYs with that diameter. We therefore find $V^*_{\mathrm{PF}} = 12.5$ for the PF conditioning (gauge length of 12 mm) and $V^*_{\mathrm{CC}} = 5$ for the CC conditioning (gauge length of 30 mm). The problem is now to define a new characteristic strength $\sigma_{0-\mathrm{op}}$ lower than σ_0 if $V^* > 1$. Since the Weibull modulus m characterizes the inhomogeneity in the population of defects population (the bigger m, the more homogeneous the population), it can be considered independent of the gauge length. In the test case ($V^* = 1$), $P_s(\sigma) = 1/e$ if $\sigma = \sigma_0$. Similarly, in the operational case ($V^* > 1$), we define $\sigma_{0-\mathrm{op}}$ such that $P_s(\sigma_{0-\mathrm{op}}) = 1/e$. This implies that $V^*(\sigma_{0-\mathrm{op}}/\sigma_0)^m = 1$, which gives:

$$\sigma_{0-\mathrm{op}} = \sigma_0 \left(V^*\right)^{-\frac{1}{m}} \tag{4}$$

Using the values of σ_0 and m from Table 3, the new $\sigma_{0-\mathrm{op}}$ for the PF conditioning decreases by 12 % with respect to σ_0 for a diameter of 10 µm and by around 25 % for diameters of 20 and 30 µm. The values decrease much more for the CC conditioning and diameters of 20 and 30 µm, due to the combination of a larger reduced volume and smaller modulus, up to a 41 % decrease for the diameter 30 µm (Table 4).

Table 4: Corrected $\sigma_{0-\mathrm{op}}$ for the calculation of the failure probability

	$\sigma_{0-\mathrm{op}}$ [MPa]	
ø	**PF**	**CC**
10	739 (-12 %)	749 (-6 %)
20	769 (-26 %)	449 (-36 %)
30	691 (-28 %)	317 (-41 %)
34	*764 (-18 %)*	-

The impact of the gauge length has also been studied by Zhang et al. on fibers composed of MWCNT of around 6-8 nm but they found that variations of the gauge length between 1 and 20 µm gave apparently randomly scattered results without any specific trend [48]. However, Wang et al., while studying CNTY transformed in rolled ribbons [55], found a large evolution of the curve

shape, with a linear increase followed by a long period of plastic deformation for 10 mm gauge length vs. almost no plastic deformation for 20 mm gauge length. Finally, the differences in strength and strain at failure were +17 % and +50 % respectively in favor of the 10 mm samples. This is slightly different with our observations, where the shape of the curves is very similar for the three diameters, with a sharp increase up to failure. As the gauge length is correlated with the copper coating, it is difficult to determine if the increase of the strain to failure of the CC conditioning is due to the gauge length or to the coating. It is particularly true if we consider the 10 µm where the variation is only 5 %.

3.3.4. Comparison of mechanical parameters

The Weibull survival probability distribution for a given stress, defined in Eq.1, is complementary to the probability of failure before that stress ($P_f(\sigma) = 1 - P_s(\sigma)$) which is itself the cumulative density function (CDF) corresponding to the following probability density function (PDF) (in the case $V^* = 1$):

$$f(\sigma) = \frac{m}{\sigma_0}\left(\frac{\sigma}{\sigma_0}\right)^{m-1} e^{-\left(\frac{\sigma}{\sigma_0}\right)^m} \tag{5}$$

On Fig 8, we plot the Weibull probability of failure before a given stress ($P_f(\sigma) = 1 - P_s(\sigma)$), first for the raw test data (Fig 8-a,b) and then for the operational WS (Fig 8-c,d) with a solid blue line for $d = 10$ µm, dotted orange line for $d = 20$ µm and dashed purple line for $d = 30$ µm. We observe that both for the PF and CC conditionings, the transition from 0 to 1 is quite sharp for $d = 10$ µm and smoother for the other two diameters. We also see that for the operational conditions, the difference between σ_0 and $\sigma_{0\text{-op}}$ shifts this transition to lower stresses, which is due to the higher number of defects in the increased volume. For the 10 µm yarns, the shift is small (11 % and 5 % for PF and CC respectively), but much larger ((46,36 %) and (28,41 %) for (PF,CC) and for $d = 20$ and 30 µm respectively. However, the slopes of the transition remain much smaller for $d = 20$ and 30 µm than for $d = 10$ µm, corresponding to a broader range of stress at failure, *i.e* an increased range of strengths for the two larger diameters.

The average strength can be computed from the PDF f defined by Eq.6, by:

$$\overline{\sigma} = \int_0^\infty \sigma f(\sigma)\,\mathrm{d}\sigma \;= \sigma_0 \Gamma\left(1 + \frac{1}{m}\right) \tag{6}$$

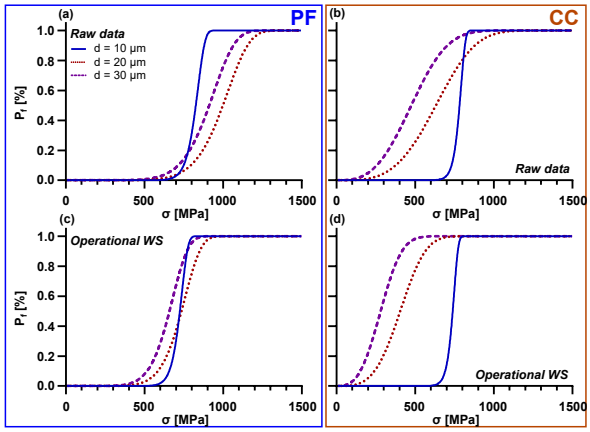

Figure 8: Probability of failure before a given stress for the PF (a) and CC conditionings (b) for $d = 10$ µm (continuous blue line), $d = 20$ µm (dotted red line) and $d = 30$ µm (purple dashed line) for the raw test data and (c and d) for the operational WS.

where Γ is the gamma special function. Results for the average strengths are summarized in Table 5, along with values for other mechanical parameters that will be discussed later. We observe that considering the length of an operational WS, Weibull analysis show a reduction of the average strength decreasing by around 10% with respect to the lengths used for the mechanical tests, for $d = 10$ µm, for both conditions. For the diameters 20 and 30 µm, the variation is much higher with 28% for d20_PF, and up to 40% for d30_CC. For comparison, we note that $\overline{\sigma}$ varies by only 20% for the $d = 34$ µm CF.

Table 5: Strain to failure (ε_{max}), maximum stress at failure (σ_{max}), average strength in the test conditions ($\overline{\sigma}_{raw}$, calculated using σ_0), average strength for operational WS ($\overline{\sigma}_{op}$, calculated using using $\sigma_{0\text{-op}}$), Young's modulus (E) and toughness (T), first for the CNTYs with $d = 10$, 20 and 30 µm, then for the 34 µm CF (only the strengths in that case).

		10 µm		**20 µm**		**30 µm**		*34 µ*
		PF	**CC**	**PF**	**CC**	**PF**	**CC**	
$\boldsymbol{\varepsilon_{max}}$	[%]	1.9 ± 0.5	1.8 ± 0.2	1.9 ± 0.2	2.4 ± 0.7	2.3 ± 0.3	3.5 ± 1.9	-
$\boldsymbol{\sigma_{max}}$	[MPa]	814 ± 65	787 ± 22	1009 ± 102	648 ± 178	918 ± 114	490 ± 164	*909* ±
$\boldsymbol{\overline{\sigma}_{raw}}$	[MPa]	820 ± 53	778 ± 35	986 ± 142	631 ± 193	900 ± 138	480 ± 172	*889* ±
$\boldsymbol{\overline{\sigma}_{op}}$	[MPa]	719 ± 46	735 ± 33	725 ± 105	405 ± 124	650 ± 99	293 ± 101	*731* ±
E	[GPa]	44 ± 14	51 ± 3	58 ± 7	26 ± 15	43 ± 11	20 ± 12	-
T	[J.g^{-1}]	5.6 ± 2.5	4.4 ± 0.4	6.7 ± 1.0	6.0 ± 2.1	7.3 ± 1.3	5.4 ± 3.1	-

The mechanisms increasing the strength of the yarn for the packing factor is mainly the reduction of the distance between CNTs and CNT bundles. Stronger bonds are created at a nano-scale for individual tubes and at a micro-scale for bundles with increasing the shear strength. This is coherent with the results of Vilatela et al. [64] where he reported the increase of yarn strength with the increase of the CNT length and so, the surfacic area in contact with other tubes. Moreover a high packing factor implies a higher probability to create entanglements between individual tubes and bundles [81]. Liu et al. observed a decrease of the strength by 45% for CNTY of 25 µm and 20 mm long with the increase of the twist angle from 12 to 38 ° [82]. An optimum twist angle of 25 ° has been observed for yarns with diameters of around 8 µm composed of MWCNT of 10 to 15 nm and 200 µm long [80]. This mechanism could explain the increase of the strength and the Young's moduli between 10 and 20 µm

3.4. In silico mechanical analysis

Particle beams at CERN take different configurations depending on the accelerator and the users. As can be seen on Fig 9-a, in the SPS, a beam, circulating at a frequency of 43375 Hz, is composed of 4 batches of protons of 1.9 µs length, spaced by 120 ns. Those batches are themselves made from 72 bunches of 1.5 ns length spaced by 25 ns. Each bunch is composed of about 10^{11} protons and has a two-dimensional gaussian distribution in the plane perpendicular to the axis of the beam. For each scan cycle, there is an acceleration of the wire during 15 ms, a flat top at the nominal speed (133 rad.s^{-1} for the fastest one, 20 m.$^{-1}$ for the linear speed) during 10 ms (during which the data acquisition is performed) and a decrease of the speed during 15 ms (Fig 9-b,c). This cycle is repeated a second time after a delay time of 150 ms for the scan out. Consequently the wire is crossed by bunches of protons, several times during the acquisition time. Since it is desirable to reduce the number of crossings in order to preserve the wire from irradiation damages, the wire speed has been increased in the new WS. However, the wire now undergoing a higher rotary acceleration, deflects and moves dynamically more from its nominal position. The accuracy of the WS measurement is thus reduced by the uncertainty on the wire position due to its vibrations. The goal is then to minimize δ, the difference between the theoretical and real position (cf. Figs.1 and 9-c), by increasing the pre-tension force during the installation of the wire in the WS, so that it deflects less. This requires

a wire material with a high tensile strength and resilience with respect to irradiation damages.

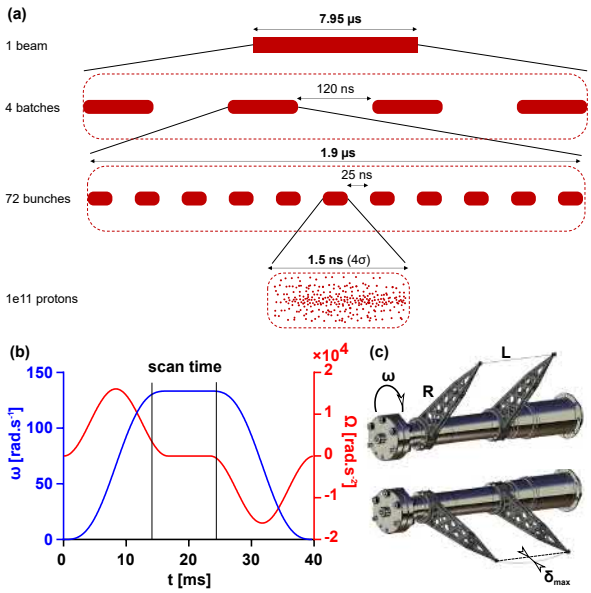

Figure 9: (a) Beam structure of the HiRadMat experiment after extraction from the SPS. The beam is structured with 4 batches spaced by 120 ns coming from the PS. Each batch are composed of 72 bunches spaced by 25 ns for a LHC beam. (b) Theoretical angular speed (in blue, left scale) and angular acceleration (in red, right scale) profiles for a SPS wire-scanner at nominal angular speed (133 rad.s^{-1}) (c) Model of the sub-assembly shaft - forks - wire and representation of the maximal deflection (δ_{max}) for a stationary state case.

The question of the optimal material to be used for the wire in the CERN WS has already been extensively studied. Materials such as beryllium [4] or carbon fibers [14] (already used at CERN for WS) or tungsten [6] (not used for fast WS) were considered. These studies have been extended for the mechanical aspect to other materials (copper, iron and titanium) [83]. Our goal in this study was to assess whether the CNTYs could stand the pre-tension imposed to reduce the uncertainty on the wire position due to its vibrations during the scan. To get the maximal deflection δ_{max}, as a function of diameter, applied load and angular scan velocity, we consider a simplified stationary model, where the wire is flying parallel around the shaft at a constant angular speed ω (details of the calculations in Annex). Thus, we neglect the transitory regime arising during the angular acceleration of the wire by supposing that its characteristic decay time is much smaller than the

10 ms of the constant angular speed phase. Thus, the accelerated phase is supposed to be there only to excite the stationary oscillations. The maximal deformation, located at the center of the wire is found to be:

$$\delta_{max} = 2R\frac{\sin^2(\frac{\alpha L}{4})}{\cos(\frac{\alpha L}{2})} \tag{7}$$

with

$$\alpha = \omega\sqrt{\frac{\rho S}{F_p}} \tag{8}$$

where R and L are the length of the forks and the wire (equal to 150 mm and 183 mm) respectively, ρ the density of the wire, and F_p the pre-tension of the wire. For existing designs, a load of 30 g is applied during assembly, corresponding to a stress of 327 MPa on current carbon fiber of 34 µm. As the installation procedures are sensitive, all the changes in the accelerator complex require in-depth studies. That is why nowadays the load has not been increased. The result for δ_max gives us an opportunity to evaluate the influence of the pre-load.

The maximal deflection is therefore plotted as a function of the pre-load for the CNTYs with diameters 10, 20 and 30 µm (density of 1.3 g.cm^{-3}, cf. subsection "Preparation of the tensile tests") and the CF of diameter 34 µm (density of 1.7 g.cm^{-3}) (Fig 10-a). We observe for all the diameters, a decrease of 80 % of the maximal deflection between 10 and 50 g of pre-load. For the same pre-load, there is a difference of 75 % between 10 and 20 µm and 90 % between 10 and 30 %. Looking at the 30 g pre-load, the maximal deflection is 4 µm, 15 µm and 34 µm for 10, 20 and 30 µm respectively. This corresponds to an applied stress $\sigma_p = F_p/S = 4F_p/(\pi d^2)$ of 2318, 777 and 356 MPa (computed with the measured real cross-sections areas: $127, 379$ and 826 µm^2 respectively). We note that the stress applied for the CNTY of diameter 10 µm is much higher than its average strength calculated previously, which would forbid us from using that diameter. However, we must remember that these results are obtained for a given pre-load while Eqs.7 and 8 show us that the important quantity is not the pre-load, but the pre-stress. As already said, in the configuration currently used, we obtain an applied stress for the 34 µm CF and 30 g of preload of 327 MPa. Using this applied stress, $\rho =$ 1.3 g.cm^{-3} and $\omega = 133$ rad.s^{-1} in Eqs.7 and 8, we get the same $\delta_{max} = 25$ µm for the CNTYs independently of the diameter, whereas using $\rho = 1.7$ g.cm^{-3} for the CF, we get $\delta_{max} = 34$ µm for the CF (Fig 10-b). Alternatively, if

we consider a preload stress equal to the previously calculated operational strength σ_{op} with a safety coefficient of 20 %, we can calculate the maximal deflection for each diameter and conditioning (Fig 10-c). Similarly to what we found for the operational strengths, we can se that the maximal deflection is roughly the same for the 3 diameters when using the PF conditioning, but much higher than for the current CF when using the CC conditioning with CNTY of diameters 20 or 30 µm, which are therefore not adequate to get a better precision on the measurement of the beam profile, than the current CF.

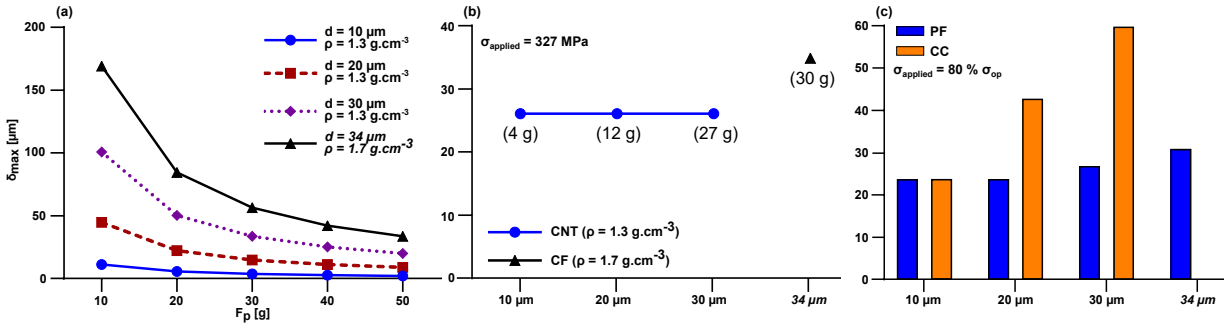

Figure 10: Maximal deflection at the center of the wire using a stationary state model (a) as a function of the pre-load for CNTYs of 10, 20 and 30 µm with density of 1.3 g.cm^{-3} and a CF with a diameter of 34 µm and density of 1.7 g.cm^{-3} (b) for an applied stress of 327 MPa and (c) considering an applied stress of 80 % of the operational strength corresponding to a given couple (diameter, conditioning).

This analysis shows the importance of a high pre-load stress during the installation in order to decrease the maximal deflection and thus increase precision of the beam profile measurement, with respect to the current CF. In our simplified model, the important quantity is the stress and not the force (in α). Hence, thinking in terms of load, as usually done, can be misleading. The comparison of the performances of the CNTYs with different diameters, for a same stress, thus seems to be more appropriate in our case. For a constant stress of 327 MPa, we observe a decrease of 25 % of the maximal deflection with respect to the current CF, for the CNTYs with $d = 10$ and 20 µm in the PF conditioning. The copper-coating seems to degrade the properties leading to a δ_{max} twice and three times larger for the 20 and 30 µm CNTYs than for the CF. However, these results have to be considered carefully, keeping in mind that the real density could be different as the one used for the calculation, and that our model relies on assumptions.

Considering the results from the Weibull analysis, we can evaluate the probability of failure for a stress of 327 MPa, for each yarn diameter and both PF and CC conditionings. Table 6 summarizes the results before and after the σ_0 correction. We observe that for $d = 10$ µm, both for the raw test data and for the operational WS, the probability of failure is quite small for both conditionings, but lower for the CC conditioning than for the PF conditionings. The behavior is partly different for $d = 20$ and 30 µm, with an increase of the failure probability P_f for the CC conditioning with respect to the PF one. However, we still have an increase of P_f for operational WS, with respect to the shorter wires used for the tests. P_f reaches 67 % for $d = 30$ µm in CC conditioning after the σ_0 correction. To have an idea of what level of probability is acceptable, we note that the current 34 µm CF have a probability of failure of $4 \cdot 10^{-4}$ % for the CF used during the mechanical tests and $4.4 \cdot 10^{-3}$ % for the operational wire.

Table 6: Probabilities (in %) of failure for a stress of 327 MPa, corresponding to a load of 30 g applied on a 34 µm CF yarn during the installation

	$\mathbf{P_f}$ **(σ = 327 MPa)**			
	Raw data		**Op WS**	
d	**PF**	**CC**	**PF**	**CC**
10	1.3e-06	1.5e-09	1.6e-05	7.6e-09
20	6.9e-03	6	8.6e-02	27
30	2.5e-02	20	3.1e-01	67
34	*4.4e-04*	-	*4.4e-3*	-

4. Conclusion

This work focused on the comparison of the mechanical properties of CNT wires between a conventional assembly of pristine wires on a paper frame and other wires copper coated at their ends. The study of the cross sections has shown that the structure of these threads is not homogeneous with, in particular, a greater packing at the core than at the surface. In addition, the overall packing seems to increase with the increase in diameter. The direct copper plating without an intermediate layer on this type of wire is a novelty and has been tested to be able to meet the current specifications of the new generation wire-scanner.

The study of the copper-coating was first of all hindered by the bad reproducibility of the samples, with very variable diameters and surface conditions which lead to much higher variations in the mechanical properties compared to the PF case. The copper / carbon interface shows copper penetration into the interstices of the wire in the surface layer. The tensile tests show an increase in the disparity of the mechanical properties with the increase in diameter. Furthermore, the mechanical strength was on average 30 % higher for the PF conditioning (910 MPa) than for the CC conditioning (640 MPa), for the three diameters. Weibull analysis also shows the importance of considering changes in the length of the sample which induces changes in σ_0 [80]. The tensile tests carried out with PF conditionings used gauge lengths of 12 mm while CC batches had gauge lengths of 30 mm and the design length for the wire to be put in the WS is 150 mm. We therefore corrected σ_0 so that the average strength and probability of failure for a given load corresponds to the same 150 mm length for all the batches. We found, as expected, that the lower the m parameter, the larger the significance of that correction on the strength results. The decrease of the scale parameter ($\sigma_{0\text{-op}}$) when shifting to a larger volume model is coherent with the increase of the number of defects and their distribution in the volume. This confirmed our observations under the microscope on the non-uniformity of the structure and the variations of the numbers and types of defects. The Weibull modulus for the batch with a 10 µm nominal diameter is much larger than for the 20 and 30 µm batches, which indicates a more uniform distribution of the defects in the structure, possibly with less defects than for the 20 and 30 µm batches. Clearly, a solution to improve the reproducibility of the copper-coating process necessary to weld the wire in the inserts of the WS must be found or the entire insertion sub-system should be redesigned.

The calculation of the failure probabilities for conventional installation loads of 10 to 50 g showed the impossibility of installing 10 µm wires with these loads without breaking them. However, our model for the maximal deflection of the wire, for a given pre-load applied during the installation of the wire, showed that the relevant quantity is not the load but the stress. For a smaller diameter, a smaller load is required to get a given stress, the failure probabilities for a given stress show a much different tendency, with the smaller diameter being the most interesting, partly due to the smaller variability of the failure stress during our tests.

The conclusion of this study is that to increase the measurement accuracy on existing instruments during scans, it will be preferable to use small

diameter wires with low density, provided they exhibit the same homogeneity of strengths than during ours tests, and that it would be useful to design a new fixing system to use pristine wires without copper coating.

5. Perspectives

In the present study, we saw (in Table 6) that the yarn that can carry the highest load is the one with the largest diameter. However, the highest tensile strengths are obtained for the 20 µm diameter. A possibility to combine these two parameters would be to braid yarns of small diameter and high mechanical resistance in order to get an equivalent diameter equal to 35 µm, which is the maximal diameter required for accelerator physics. This would lead to increase the cross-section of the new yarn, keeping the best mechanical properties of the fibers. A braiding machine prototype has been developed at CERN and the first braided yarns have been created using 100 µm CNTYs. Mechanical tests will be performed on these new braided yarns to assess their strength distribution.

In the old WS we used carbon fibers. This kind of material has been extensively used in research and industry. This has led to a good understanding of their mechanical properties. On the contrary, the development of CNTYs is more recent, and little is known about their properties, especially for applications in beam instrumentation which are very rare [84, 85]. Previous studies of these wires after proton [86], ions [87], electrons [88, 89] or gamma ray irradiation [90, 91] at low energies showed an improvement of mechanical resistance under certain conditions, possibly due to the creation of chemical bonds between layers of CNTs or between CNTs themselves. However, we currently have no results at very high energies - GeV / TeV. This is why projects are currently ongoing to irradiate CNTYs in the SPS at CERN, with protons of 450 GeV and integrated intensity of 3.2×10^{15} particles. Post irradiation analysis should give some answers concerning the evolution of their mechanical properties (and survival probability) under such harsh conditions.

6. Authorship contribution statements

A. Mariet: Conceptualization, Methodology, Software, Formal analysis, Investigation, Writing – original draft, Visualization. **A. T. Perez Fontenla:** Resources, Writing - Original Draft. **X. Gabrion:** Resources,

Writing - Original Draft. **C. Salomon:** Software, Formal analysis. **M. Devel:** Resources, Visualization, Supervision, Writing - Review & Editing. **R. Veness:** Resources, Visualization, Supervision, Writing - Review & Editing

7. Acknowledgments

The authors would like to thank H.R. Jauslin from the University of Bourgogne for the very helpful discussions and acknowledge, the CNTY provider T. Inoue, N. Morihara and Hitachi Zosen Co, and M. Hamani for the technical support and sample preparation. This work was supported by the "Investissements d'Avenir" program EUR-EIPHI Graduate School (Grant No. 17-EURE-0002). The authors would like to acknowledge all the persons who contributed to this paper, the FCC project and CERN doctoral program for the founding.

8. Annex: calculation of the maximum deflection of the wire as a function of pre-load

We consider that the attachment points $(x = 0, y = 0)$ and $(x = L, y = 0)$, where the wire is welded on the forks, are at a distance R from the axis of rotation. The model is then a linear wave equation for a vibrating string of length L, submitted to the centrifugal force produced by a rotation of angular velocity $\omega = v_{scan}/R$ and a tensile pre-load F_p applied to the wire during the installation.

The equation of motion for the string in the rotating frame is then: [92]:

$$\frac{\partial^2 y(x,t)}{\partial t^2} = \frac{F_p}{\lambda}\frac{\partial^2 y(x,t)}{\partial x^2} + \omega^2(R + y(x,t)) \tag{9}$$

$$\begin{gathered}\text{Boundary conditions}\\ y(x=0,t)=0\\ y(x=L,t)=0\\ \text{Initial conditions}\\ y(x,t_0)=f(t_0)\\ \frac{\partial y}{\partial t}(x,t_0)=f'(t_0)\end{gathered}$$

with λ the linear density defined as $\lambda = \rho S$, with ρ the bulk density and S the cross-section of the wire. The stationary state is thus determined by the equation:

$$\frac{\partial^2 y_{stat}(x)}{\partial x^2} + \alpha^2 y_{stat}(x) = -\alpha^2 R \tag{10}$$

with $\alpha = \omega\sqrt{\lambda/F_p} = \omega\sqrt{\rho/\sigma_p}$. Eq. 10 is an inhomogeneous linear ordinary differential equation with constant coefficients that can be solved explicitly in terms of trigonometric functions. The solution can be written as

$$y_{stat}(x) = 2R\frac{\sin(\frac{\alpha x}{2})\sin(\frac{\alpha(L-x)}{2})}{\cos(\frac{\alpha L}{2})} \tag{11}$$

References

[1] H. Bartosik, G. Rumolo, Review of LIU beam parameter table: protons (2012).
URL https://indico.cern.ch/event/557356/contributions/2246280/attachments/1327239/1993693/2016.08.26_LIU-beam-parameters-update.pdf

[2] The HL-LHC project | High Luminosity LHC Project (2020).
URL https://hilumilhc.web.cern.ch/content/hl-lhc-project

[3] The FCC collaboration | FCC-hh: The Hadron Collider, The European Physical Journal Special Topics 228 (4) (2019) 755–1107. doi:10.1140/epjst/e2019-900087-0.
URL https://doi.org/10.1140/epjst/e2019-900087-0

[4] C. Fischer, A study of a wire scanner for lep (1986).
URL https://cds.cern.ch/record/169603/files/SCAN-0008008.pdf

[5] J. Bosser, J. Camas, L. Evans, G. Ferioli, J. Mann, R. Olsen, R. Schmidt, The micron wire scanner at the SPS, CERNSPS-Div-Rep-87-13-ABM, CERN, Geneva (1987).

[6] C. Field, D. McCormick, P. Raimondi, M. Ross, Wire breakage in slc wire profile monitors, AIP Conference Proceedings 451 (1) (1998) 440–445. arXiv:https://aip.scitation.org/doi/pdf/10.1063/1.57029, doi:10.1063/1.57029.
URL https://aip.scitation.org/doi/abs/10.1063/1.57029

[7] A. Burns, J. Camas, E. D'Amico, G. Ferioli, Q. King, K. H. Kissler, J. Mann, R. Schmidt, Wire scanner news from the CERN-SPS, in:

Proceedings of the 1989 IEEE Particle Accelerator Conference, . 'Accelerator Science and Technology, 1989, pp. 1580–1582 vol.3. doi:10.1109/PAC.1989.72857.

[8] P. Krejcik, M. Campell, J. D'Ewart, H. Loos, K. Luchini, Performance of the new fast wire scanner at the LCLS, in: Proceedings of the 4th International Beam Instrumentation Conference (IBIC2015), 2016, pp. 547–549.

[9] J. M. D'Ewart, M. Campell, P. Krejcik, H. Loos, K. Luchini, Fast wire scanner upgrade for LCLS (2016).
URL https://accelconf.web.cern.ch/ICALEPCS2015/papers/mopgf015.pdf

[10] Q. King, Analysis of the Influence of Fibre Diameter on Wirescanner Beam Profile Measurements (1988).
URL https://cds.cern.ch/record/2201587

[11] J. Bosser, C. Bovet, Wire scanners for LHC, Tech. rep., CERN-LHC-Project-Note-108 (1997).

[12] J. Camas, C. Fischer, J. J. Gras, R. Jung, J. Koopman, Observation of thermal effects on the LEP wire scanners, in: Proceedings Particle Accelerator Conference, Vol. 4, 1995, pp. 2649–2651 vol.4. doi:10.1109/PAC.1995.505647.

[13] M. Brice, A fast wire scanner, used to measure the transverse density distribution of beams circulating in an accelerator or storage ring., number: CERN-EX-0205022 (May 2002).
URL https://cds.cern.ch/record/43035

[14] M. Sapinski, Model of Carbon Wire Heating in Accelerator Beam (Jul. 2008).
URL https://cds.cern.ch/record/1123363

[15] M. Sapinski, J. Koopman, E. Métral, A. Guerrero, B. Dehning, Carbon Fiber Damage in Accelerator Beam (May 2009).
URL https://cds.cern.ch/record/1183415

[16] B. Dehning, T. Kroyer, M. Meyer, M. Sapinski, A. Guerrero, Carbon Fiber Damage in Particle Beam (Sep. 2010).
URL https://cds.cern.ch/record/1348020

[17] R. Veness, J. Emery, J. Sirvent, J. Tassan-Viol, N. Chritin, B. Dehning, D. Gudkov, P. Andersson, F. Roncarolo, W. Andreazza, A. Goldblatt, Installation and Test of Pre-series Wire Scanners for the LHC Injector Upgrade Project at CERN, library Catalog: cds.cern.ch Number: CERN-ACC-2017-199 Pages: MOPAB121 (2017). doi:10.18429/JACoW-IPAC2017-MOPAB121.
URL https://cds.cern.ch/record/2289486

[18] J. Sirvent, P. Andersson, W. Andreazza, B. Dehning, J. Emery, L. Garcia, D. Gudkov, F. Roncarolo, J. Tassan-Viol, G. Trad, R. Veness, Performance Assessment of Pre-Series Fast Beam Wire Scanner Prototypes for the Upgrade of the CERN LHC Injector Complex, Proceedings of the 6th Int. Beam Instrumentation Conf. IBIC2017 (2018) 4 pages, 1.081 MB. doi:10.18429/JACOW-IBIC2017-WEPCC03.

[19] R. Veness, W. Andreazza, N. Chritin, B. Dehning, J. Emery, D. Gudkov, J. Herranz, P. Magagnin, E. Piselli, S. Samuelsson, Experience from the construction of a new fast wire scanner prototype for the CERN-SPS and its optimisation for installation in the CERN-PS booster, in: 4th International Beam Instrumentation Conference (IBIC2015), JACOW, Geneva, Switzerland, Melbourne, Australia, 2016, pp. 479–482.

[20] J. Herranz, W. Andreazza, A. Barjau, N. Chritin, B. Dehning, J. Emery, D. Gudkov, P. Magagnin, S. Samuelsson, J. Sirvent, The 20m/s CERN Fast Vacuum Wire Scanner Conceptual Design and Implementation, in: 9th Edition of the Mechanical Engineering Design of Synchrotron Radiation Equipment and Instrumentation Conference (MEDSI'16), Barcelona, Spain, 11-16 September 2016, JACOW Publishing, Geneva, Switzerland, 2017, pp. 29–31.

[21] L. Radushkevich, V. Lukyanovich, About the structure of carbon formed by thermal decomposition of carbon monoxide on iron substrate, J. Phys. Chem.(Moscow) 26 (1952) 88–95.

[22] S. Iijima, Helical microtubules of graphitic carbon, Nature 354 (6348)

(1991) 56. doi:10.1038/354056a0.
URL https://www.nature.com/articles/354056a0

[23] B. I. Yakobson, R. E. Smalley, Fullerene nanotubes: C 1,000,000 and beyond: Some unusual new molecules—long, hollow fibers with tantalizing electronic and mechanical properties—have joined diamonds and graphite in the carbon family, American Scientist 85 (4) (1997) 324–337.
URL http://www.jstor.org/stable/27856810

[24] M.-F. Yu, O. Lourie, M. J. Dyer, K. Moloni, T. F. Kelly, R. S. Ruoff, Strength and Breaking Mechanism of Multiwalled Carbon Nanotubes Under Tensile Load, Science 287 (5453) (2000) 637–640. doi:10.1126/science.287.5453.637.
URL https://science.sciencemag.org/content/287/5453/637

[25] X. Zhang, Q. Li, T. G. Holesinger, P. N. Arendt, J. Huang, P. D. Kirven, T. G. Clapp, R. F. DePaula, X. Liao, Y. Zhao, L. Zheng, D. E. Peterson, Y. Zhu, Ultrastrong, Stiff, and Lightweight Carbon-Nanotube Fibers, Advanced Materials 19 (23) (2007) 4198–4201. doi:10.1002/adma.200700776.
URL https://onlinelibrary.wiley.com/doi/abs/10.1002/adma.200700776

[26] P. Avouris, Carbon nanotube electronics, Chemical Physics 281 (2) (2002) 429–445. doi:https://doi.org/10.1016/S0301-0104(02)00376-2.
URL https://www.sciencedirect.com/science/article/pii/S0301010402003762

[27] A. Allaoui, S. Bai, H. M. Cheng, J. B. Bai, Mechanical and electrical properties of a MWNT/epoxy composite, Composites Science and Technology 62 (15) (2002) 1993–1998. doi:10.1016/S0266-3538(02)00129-X.
URL http://www.sciencedirect.com/science/article/pii/S026635380200129X

[28] M.-Y. Tsai, C.-Y. Yu, C.-H. Yang, N.-H. Tai, T.-P. Perng, C.-M. Tu, Z. H. Khan, Y.-C. Liao, C. C. Chi, Electrical transport properties of individual disordered multiwalled carbon nanotubes, Applied Physics

Letters 89 (19) (2006) 192115. doi:10.1063/1.2387875.
URL https://doi.org/10.1063/1.2387875

[29] S. Li, X. Zhang, J. Zhao, F. Meng, G. Xu, Z. Yong, J. Jia, Z. Zhang, Q. Li, Enhancement of carbon nanotube fibres using different solvents and polymers, Composites Science and Technology 72 (12) (2012) 1402–1407. doi:10.1016/j.compscitech.2012.05.013.
URL http://www.sciencedirect.com/science/article/pii/S026635381200200X

[30] K. Sun, M. A. Stroscio, M. Dutta, Thermal conductivity of carbon nanotubes, Journal of Applied Physics 105 (7) (2009) 074316. doi:10.1063/1.3095759.
URL https://aip.scitation.org/doi/abs/10.1063/1.3095759

[31] S. Berber, Y. Kwon, D. Tománek, Unusually High Thermal Conductivity of Carbon Nanotubes, Physical Review Letters 84 (20) (2000) 4613–4616. doi:10.1103/PhysRevLett.84.4613.
URL https://link.aps.org/doi/10.1103/PhysRevLett.84.4613

[32] J. Che, T. Çagin, W. A. Goddard, Thermal conductivity of carbon nanotubes, Nanotechnology 11 (2) (2000) 65–69. doi:10.1088/0957-4484/11/2/305.
URL https://doi.org/10.1088%2F0957-4484%2F11%2F2%2F305

[33] C. Laurent, E. Flahaut, A. Peigney, The weight and density of carbon nanotubes versus the number of walls and diameter, Carbon 48 (10) (2010) 2994–2996. doi:10.1016/j.carbon.2010.04.010.
URL http://www.sciencedirect.com/science/article/pii/S0008622310002617

[34] Y.-L. Li, I. A. Kinloch, A. H. Windle, Direct Spinning of Carbon Nanotube Fibers from Chemical Vapor Deposition Synthesis, Science 304 (5668) (2004) 276–278, publisher: American Association for the Advancement of Science Section: Report. doi:10.1126/science.1094982.
URL https://science.sciencemag.org/content/304/5668/276

[35] W. Liu, X. Zhang, G. Xu, P. D. Bradford, X. Wang, H. Zhao, Y. Zhang, Q. Jia, F.-G. Yuan, Q. Li, Y. Qiu, Y. Zhu, Producing superior composites by winding carbon nanotubes onto a mandrel

under a poly(vinyl alcohol) spray, Carbon 49 (14) (2011) 4786–4791. doi:10.1016/j.carbon.2011.06.089.
URL http://www.sciencedirect.com/science/article/pii/S0008622311005367

[36] Y. Inoue, K. Kakihata, Y. Hirono, T. Horie, A. Ishida, H. Mimura, One-step grown aligned bulk carbon nanotubes by chloride mediated chemical vapor deposition, Applied Physics Letters 92 (21) (2008) 213113, publisher: American Institute of Physics. doi:10.1063/1.2937082.
URL https://aip.scitation.org/doi/full/10.1063/1.2937082

[37] S. P. Patole, P. S. Alegaonkar, H.-C. Shin, J.-B. Yoo, Alignment and wall control of ultra long carbon nanotubes in water assisted chemical vapour deposition, fabrication, Journal of Physics D: Applied Physics 41 (15) (2008) 155311. doi:10.1088/0022-3727/41/15/155311.
URL https://doi.org/10.1088/0022-3727/41/15/155311

[38] A. Ghemes, Y. Minami, J. Muramatsu, M. Okada, H. Mimura, Y. Inoue, Fabrication and mechanical properties of carbon nanotube yarns spun from ultra-long multi-walled carbon nanotube arrays, Carbon 50 (12) (2012) 4579–4587. doi:10.1016/j.carbon.2012.05.043.

[39] H. Choo, Y. Jung, Y. Jeong, H. C. Kim, B.-C. Ku, Fabrication and Applications of Carbon Nanotube Fibers, Carbon letters 13 (4) (2012) 191–204, publisher: Korean Carbon Society. doi:10.5714/CL.2012.13.4.191.
URL http://www.koreascience.or.kr/article/JAKO201214350262751.page

[40] P. Sharma, P. Ahuja, Recent advances in carbon nanotube-based electronics, Materials Research Bulletin 43 (10) (2008) 2517–2526. doi:https://doi.org/10.1016/j.materresbull.2007.10.012.
URL https://www.sciencedirect.com/science/article/pii/S0025540807004564

[41] J. N. Coleman, U. Khan, W. J. Blau, Y. K. Gun'ko, Small but strong: A review of the mechanical properties of carbon nanotube–polymer composites, Carbon 44 (9) (2006) 1624–1652. doi:10.1016/j.carbon.2006.02.038.

URL http://www.sciencedirect.com/science/article/pii/S0008622306001229

[42] X. Wei, M. Naraghi, H. D. Espinosa, Optimal Length Scales Emerging from Shear Load Transfer in Natural Materials: Application to Carbon-Based Nanocomposite Design, ACS Nano 6 (3) (2012) 2333–2344, publisher: American Chemical Society. doi:10.1021/nn204506d.
URL https://doi.org/10.1021/nn204506d

[43] A. Mikhalchan, M. Ridha, T. Tay, Carbon nanotube fibres for cfrp-hybrids with enhanced in-plane fracture behaviour, Materials & Design 143 (2018) 112–119. doi:https://doi.org/10.1016/j.matdes.2018.01.053.
URL https://www.sciencedirect.com/science/article/pii/S0264127518300674

[44] Q. W. Li, X. F. Zhang, R. F. DePaula, L. X. Zheng, Y. H. Zhao, L. Stan, T. G. Holesinger, P. N. Arendt, D. E. Peterson, Y. T. Zhu, Sustained Growth of Ultralong Carbon Nanotube Arrays for Fiber Spinning, Advanced Materials 18 (23) (2006) 3160–3163. doi:10.1002/adma.200601344.
URL https://onlinelibrary.wiley.com/doi/abs/10.1002/adma.200601344

[45] L. M. Ericson, H. Fan, H. Peng, V. A. Davis, W. Zhou, J. Sulpizio, Y. Wang, R. Booker, J. Vavro, C. Guthy, A. N. G. Parra-Vasquez, M. J. Kim, S. Ramesh, R. K. Saini, C. Kittrell, G. Lavin, H. Schmidt, W. W. Adams, W. E. Billups, M. Pasquali, W.-F. Hwang, R. H. Hauge, J. E. Fischer, R. E. Smalley, Macroscopic, Neat, Single-Walled Carbon Nanotube Fibers, Science 305 (5689) (2004) 1447–1450, publisher: American Association for the Advancement of Science Section: Report. doi:10.1126/science.1101398.
URL https://science.sciencemag.org/content/305/5689/1447

[46] Y. Yang, L. Liu, K. Jiang, S. Fan, A vacuum sensor using field emitters made by multiwalled carbon nanotube yarns, Vacuum 86 (7) (2012) 885–888, selected papers from the IUVSTA 18th International Vacuum Congress (IVC-18) held in Beijing, P.R.China, 23 -27 August 2010. doi:https://doi.org/10.1016/j.vacuum.2011.04.027.

URL https://www.sciencedirect.com/science/article/pii/S0042207X11001710

[47] J. J. Vilatela, A. H. Windle, A Multifunctional Yarn Made of Carbon Nanotubes, Journal of Engineered Fibers and Fabrics 7 (2_suppl) (2012) 155892501200702S04, publisher: SAGE Publications Ltd STM. doi:10.1177/155892501200702S04.

[48] Y. Zhang, L. Zheng, G. Sun, Z. Zhan, K. Liao, Failure mechanisms of carbon nanotube fibers under different strain rates, Carbon 50 (8) (2012) 2887–2893. doi:10.1016/j.carbon.2012.02.057.

[49] H. Kim, S. J. Kim, High toughness of bio-inspired multi-strand coiled carbon nanotube yarn, Carbon 131 (2018) 60–65. doi:10.1016/j.carbon.2018.01.048.
URL https://www.sciencedirect.com/science/article/pii/S0008622318300575

[50] X. Liang, Y. Gao, J. Duan, Z. Liu, S. Fang, R. H. Baughman, L. Jiang, Q. Cheng, Enhancing the strength, toughness, and electrical conductivity of twist-spun carbon nanotube yarns by pi bridging, Carbon 150 (2019) 268–274. doi:10.1016/j.carbon.2019.05.023.

[51] W. Li, J. Zhao, Y. Xue, X. Ren, X. Zhang, Q. Li, Merge multiple carbon nanotube fibers into a robust yarn, Carbon 145 (2019) 266–272. doi:10.1016/j.carbon.2019.01.054.
URL http://www.sciencedirect.com/science/article/pii/S0008622319300545

[52] O.-K. Park, H. Choi, H. Jeong, Y. Jung, J. Yu, J. K. Lee, J. Y. Hwang, S. M. Kim, Y. Jeong, C. R. Park, M. Endo, B.-C. Ku, High-modulus and strength carbon nanotube fibers using molecular cross-linking, Carbon 118 (2017) 413–421. doi:10.1016/j.carbon.2017.03.079.
URL http://www.sciencedirect.com/science/article/pii/S0008622317303354

[53] Y.-O. Im, S.-H. Lee, T. Kim, J. Park, J. Lee, K.-H. Lee, Utilization of carboxylic functional groups generated during purification of carbon nanotube fiber for its strength improvement, Applied Surface Science 392 (2017) 342–349. doi:10.1016/j.apsusc.2016.09.060.

URL http://www.sciencedirect.com/science/article/pii/S0169433216319298

[54] C. Jiang, X. Yang, J. Zhao, Q. Li, K.-Q. Zhang, X. Zhang, Q. Li, Densifying carbon nanotubes on assembly surface by the self-contraction of silk fibroin, Applied Surface Science 436 (2018) 66–72. doi:10.1016/j.apsusc.2017.12.005.

[55] J. N. Wang, X. G. Luo, T. Wu, Y. Chen, High-strength carbon nanotube fibre-like ribbon with high ductility and high electrical conductivity, Nature Communications 5 (1) (2014) 1–8. doi:10.1038/ncomms4848.

[56] M. Miao, The role of twist in dry spun carbon nanotube yarns, Carbon 96 (2016) 819–826. doi:10.1016/j.carbon.2015.10.022.
URL http://www.sciencedirect.com/science/article/pii/S0008622315303481

[57] C. Du, N. Pan, CVD growth of carbon nanotubes directly on nickel substrate, Materials Letters 59 (13) (2005) 1678–1682. doi:10.1016/j.matlet.2005.01.043.
URL http://www.sciencedirect.com/science/article/pii/S0167577X05000881

[58] M. J. Bronikowski, Cvd growth of carbon nanotube bundle arrays, Carbon 44 (13) (2006) 2822–2832. doi:https://doi.org/10.1016/j.carbon.2006.03.022.
URL https://www.sciencedirect.com/science/article/pii/S0008622306001667

[59] O. Yaglioglu, A. Cao, A. J. Hart, R. Martens, A. H. Slocum, Wide range control of microstructure and mechanical properties of carbon nanotube forests: A comparison between fixed and floating catalyst cvd techniques, Advanced Functional Materials 22 (23) (2012) 5028–5037. arXiv:https://onlinelibrary.wiley.com/doi/pdf/10.1002/adfm.201200852, doi:https://doi.org/10.1002/adfm.201200852.
URL https://onlinelibrary.wiley.com/doi/abs/10.1002/adfm.201200852

[60] T. Tezuka, N. Mori, T. Murayama, T. Sano, T. Nakagawa, H. Inoue, Y. Hayashi, T. Kuzumaki, Nanostructural characterization of carbon

nanotube yarn high-strengthened by joule heating, Carbon 171 (2021) 437 – 443. doi:https://doi.org/10.1016/j.carbon.2020.09.014.
URL http://www.sciencedirect.com/science/article/pii/S0008622320308629

[61] T. Kluyver, B. Ragan-Kelley, F. Pérez, B. Granger, M. Bussonnier, J. Frederic, K. Kelley, J. Hamrick, J. Grout, S. Corlay, P. Ivanov, D. Avila, S. Abdalla, C. Willing, Jupyter notebooks – a publishing format for reproducible computational workflows, in: F. Loizides, B. Schmidt (Eds.), Positioning and Power in Academic Publishing: Players, Agents and Agendas, IOS Press, 2016, pp. 87 – 90.

[62] C. A. Schneider, W. S. Rasband, K. W. Eliceiri, NIH Image to ImageJ: 25 years of image analysis, Nature Methods 9 (7) (2012) 671–675. doi:10.1038/nmeth.2089.
URL https://www.nature.com/articles/nmeth.2089

[63] Inkscape Project, Inkscape.
URL https://inkscape.org

[64] J. J. Vilatela, J. A. Elliott, A. H. Windle, A Model for the Strength of Yarn-like Carbon Nanotube Fibers, ACS Nano 5 (3) (2011) 1921–1927. doi:10.1021/nn102925a.

[65] A. Mikhalchan, J. J. Vilatela, A perspective on high-performance cnt fibres for structural composites, Carbon 150 (2019) 191–215. doi:https://doi.org/10.1016/j.carbon.2019.04.113.
URL https://www.sciencedirect.com/science/article/pii/S0008622319304567

[66] K. Sugano, M. Kurata, H. Kawada, Evaluation of mechanical properties of untwisted carbon nanotube yarn for application to composite materials, Carbon 78 (2014) 356–365.

[67] M. Zhang, K. R. Atkinson, R. H. Baughman, Multifunctional Carbon Nanotube Yarns by Downsizing an Ancient Technology, Science 306 (5700) (2004) 1358–1361, publisher: American Association for the Advancement of Science Section: Report. doi:10.1126/science.1104276.
URL https://science.sciencemag.org/content/306/5700/1358

[68] M. Miao, J. McDonnell, L. Vuckovic, S. C. Hawkins, Poisson's ratio and porosity of carbon nanotube dry-spun yarns, Carbon 48 (10) (2010) 2802–2811. doi:10.1016/j.carbon.2010.04.009.
URL http://www.sciencedirect.com/science/article/pii/S0008622310002605

[69] M. G. Hahm, J.-H. Lee, A. H. C. Hart, S. M. Song, J. Nam, H. Y. Jung, D. P. Hashim, B. Li, T. N. Narayanan, C.-D. Park, Y. Zhao, R. Vajtai, Y. A. Kim, T. Hayashi, B.-C. Ku, M. Endo, E. Barrera, Y. J. Jung, E. L. Thomas, P. M. Ajayan, Carbon Nanotube Core Graphitic Shell Hybrid Fibers, ACS Nano 7 (12) (2013) 10971–10977, publisher: American Chemical Society. doi:10.1021/nn4045276.
URL https://doi.org/10.1021/nn4045276

[70] M. Kaminski, F. Laurin, J. F. Maire, R. Desmorat, Modélisation de la durée de vie des matériaux composites CMO (Jan. 2017).

[71] J. Jia, J. Zhao, G. Xu, J. Di, Z. Yong, Y. Tao, C. Fang, Z. Zhang, X. Zhang, L. Zheng, Q. Li, A comparison of the mechanical properties of fibers spun from different carbon nanotubes, Carbon 49 (4) (2011) 1333–1339. doi:10.1016/j.carbon.2010.11.054.

[72] J. C. Fernández-Toribio, A. Mikhalchan, C. Santos, Álvaro Ridruejo, J. J. Vilatela, Understanding cooperative loading in carbon nanotube fibres through in-situ structural studies during stretching, mechanical, Carbon 156 (2020) 430–437. doi:https://doi.org/10.1016/j.carbon.2019.09.070.
URL https://www.sciencedirect.com/science/article/pii/S0008622319309789

[73] L. N. McCartney, R. L. Smith, Statistical Theory of the Strength of Fiber Bundles, Journal of Applied Mechanics 50 (3) (1983) 601–608. doi:10.1115/1.3167097.
URL https://doi.org/10.1115/1.3167097

[74] P. Jiang, Y. Xing, X. Jia, B. Guo, Weibull Failure Probability Estimation Based on Zero-Failure Data, Mathematical Problems in Engineering 2015 (2015) e681232. doi:10.1155/2015/681232.
URL https://www.hindawi.com/journals/mpe/2015/681232/

[75] N. M. Pugno, R. S. Ruoff, Nanoscale weibull statistics, Journal of Applied Physics 99 (2) (2006) 024301. arXiv:https://doi.org/10.1063/1.2158491, doi:10.1063/1.2158491.
URL https://doi.org/10.1063/1.2158491

[76] D. L. Naik, T. H. Fronk, Weibull distribution analysis of the tensile strength of the kenaf bast fiber, Fibers and Polymers 17 (10) (2016) 1696–1701. doi:10.1007/s12221-016-6176-6.
URL https://doi.org/10.1007/s12221-016-6176-6

[77] C. Zweben, The effect of stress nonuniformity and size on the strength of composite materials, Journal of Composites, Technology and Research 3 (1) (1981) 23–26.

[78] B. Redjel, F. X. De Charentenay, Application des statistiques de Weibull à la caractérisation des résines phénoliques et des matériaux composites SMC, Matériaux & Techniques 75 (10-11) (1987) 421–424.

[79] B. Redjel, Utilisation du modèle probabiliste de Weibull à la caractérisation de l'aspect aléatoire de la rupture en traction de panneaux en bois à lamelles orientées OSB., in: Congrès français de mécanique, AFM, Association Française de Mécanique, 2017.

[80] Y. Sugimoto, M. Shioya, H. Matsumoto, M. Minagawa, A. Tanioka, Structure changes during tensile deformation and mechanical properties of a twisted carbon nanotube yarn, Carbon 60 (2013) 193 – 201. doi:https://doi.org/10.1016/j.carbon.2013.03.064.
URL http://www.sciencedirect.com/science/article/pii/S0008622313003072

[81] C. Tran, W. Humphries, S. Smith, C. Huynh, S. Lucas, Improving the tensile strength of carbon nanotube spun yarns using a modified spinning process, Carbon 47 (11) (2009) 2662 – 2670. doi:https://doi.org/10.1016/j.carbon.2009.05.020.

[82] K. Liu, Y. Sun, R. Zhou, H. Zhu, J. Wang, L. Liu, S. Fan, K. Jiang, Carbon nanotube yarns with high tensile strength made by a twisting and shrinking method, Nanotechnology 21 (4) (2009) 045708. doi:10.1088/0957-4484/21/4/045708.

[83] A. Mariet, R. Veness, Selection of Wires for the New Generation of Fast Wire Scanners at CERN (2019) WEPC19doi:10.18429/JACoW-IBIC2018-WEPC19.

[84] T. Miyao, A. Miura, Beam profile measurement using carbon nanotube wires (2017).

[85] A. Miura, T. Miyao, K. Moriya, Application of carbon nanotube wire for beam profile measurement of negative hydrogen ion beam, in: Proc. 9th Int. Particle Accelerator Conf IPAC18, JACOW Publishing, Geneva, Switzerland, Vancouver, Canada, 2018, pp. 5022–5025.

[86] J. G. Gigax, P. D. Bradford, L. Shao, Radiation-induced mechanical property changes of cnt yarn, Nuclear Instruments and Methods in Physics Research Section B: Beam Interactions with Materials and Atoms 409 (2017) 268 – 271, proceedings of the 20th International Conference on Ion Beam Modification of Materials (IBMM 2016). doi:https://doi.org/10.1016/j.nimb.2017.04.050.
URL http://www.sciencedirect.com/science/article/pii/S0168583X17305001

[87] J. G. Gigax, P. D. Bradford, L. Shao, Ion beam modification of carbon nanotube yarn in air and vacuum, Materials (Basel, Switzerland) 10 (8) (July 2017). doi:10.3390/ma10080860.
URL https://europepmc.org/articles/PMC5578226

[88] B. Peng, M. Locascio, P. Zapol, S. Li, S. L. Mielke, G. C. Schatz, H. D. Espinosa, Measurements of near-ultimate strength for multiwalled carbon nanotubes and irradiation-induced crosslinking improvements, Nature Nanotechnology 3 (10) (2008) 626–631. doi:10.1038/nnano.2008.211.
URL https://www.nature.com/articles/nnano.2008.211

[89] T. Filleter, R. Bernal, S. Li, H. D. Espinosa, Ultrahigh Strength and Stiffness in Cross-Linked Hierarchical Carbon Nanotube Bundles, Advanced Materials 23 (25) (2011) 2855–2860, _eprint: https://onlinelibrary.wiley.com/doi/pdf/10.1002/adma.201100547.
doi:10.1002/adma.201100547.

[90] V. Skákalová, M. Hulman, P. Fedorko, P. Lukáč, S. Roth, Effect Of Gamma-Irradiation on Single-Wall Carbon Nanotube Paper, AIP Conference Proceedings 685 (1) (2003) 143–147. doi:10.1063/1.1628005.

[91] M. Miao, S. C. Hawkins, J. Y. Cai, T. R. Gengenbach, R. Knott, C. P. Huynh, Effect of gamma-irradiation on the mechanical properties of carbon nanotube yarns, Carbon 49 (14) (2011) 4940–4947. doi:10.1016/j.carbon.2011.07.026.
URL http://www.sciencedirect.com/science/article/pii/S0008622311005872

[92] H. F. Weinberger, A First Course in Partial Differential Equations: with Complex Variables and Transform Methods, Courier Corporation, 2012, Ch. 1, pp. 1–8, google-Books-ID: Ay11RfO3jGgC.